A parametric study of serration design for trailing–edge broadband noise reduction

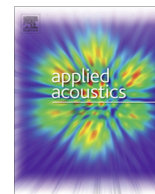Lima Pereira, Lourenço Tércio; Avallone, Francesco; Ragni, Daniele; Scarano, Fulvio

Important note
To cite this publication, please use the final published version (if applicable).
Please check the document version above.

A parametric study of serration design for trailing–edge broadband noise reduction

Lourenço Tércio Lima Pereira [a,*], Francesco Avallone [a,b], Daniele Ragni [a], Fulvio Scarano [a]

[s] Faculty of Aerospace Engineering, Delft University of Technology, Kluyverweg 1, Delft 2629HS, The Netherlands
[b] Politecnico di Torino, Dipartimento di INGEGNERIA MECCANICA E AEROSPAZIALE (DIMEAS)

ARTICLE INFO

ABSTRACT

This work discusses the physics of noise reduction achieved from serrated trailing–edges and its impact by the serration design. An experimental campaign is carried out with a benchmark 2D model based on a NACA 63_3–018 airfoil. Different trailing-edge serrations are tested under several flow speeds and angles of attack conditions to build a complete dataset of acoustic measurements. Systematic modifications of a reference sawtooth serration design are made to its scale and geometry. Scale modifications are based on sawtooth serrations and comprehend carefully considered variations of the serration height ($2h$), wavenumber (λ), and aspect ratio ($2h/\lambda$). Geometric shape modifications are represented by concave–shaped and combed–sawtooth serrations. This study represents a unique sensitivity–based parametric analysis on the scaling and geometric properties of trailing–edge serrations where the impacts of each modification are studied separately. The results obtained are used to provide guidelines for serration design choices and their impact on broadband noise reduction.

1. Introduction

Trailing–edge serrations are currently the standard technology applied to mitigate the noise generated by the turbulent boundary-layer flow past an airfoil trailing edge. Industrial applications, such as wind energy [1,2] and turbo machinery [3], have adopted serrations as they provide significant noise reduction [1]. However, their proven efficiency and applicability contrasts with the current design methods for such device. This is due to the discrepancies observed between theoretical predictions and results from experimental campaigns and numerical simulations.

Theoretical models [4–8] have described the main physical mechanism of serrated trailing edges and explained the noise reduction obtained. According to the theory, by creating a non-orthogonal angle between the incoming turbulent flow fluctuations and the trailing-edge direction, serrations promote a weaker scattering of the dominant wall-pressure fluctuation modes, i.e. the spanwise oriented waves ($k_z = 0$). Similarly to the noise of a slanted trailing edge [9], this weaker scattering in comparison to a straight edge is responsible for the noise reduction observed in the far field.

The analytical approaches, however, neglect the modifications of the flow due to the presence of the serrations which, in turn, affect the acoustic response [10–12]. Throughout the years, researchers have demonstrated that the flow is significantly altered by introducing trailing–edge serrations [13–18]. In an effort to model such alterations, Ref. [17] has shown that three physical mechanisms dominate the modification of the wall–pressure fluctuations on the surface of a serrated trailing edge. Two of these mechanisms concern the alteration of conditions in the vicinity of the serrations while the last one pertains only to serrations generating aerodynamic loading, i.e. a pressure difference between the upper and lower side of the serration exists. This aerodynamic loading causes a pair of counter–rotating vortices to be formed around the serration edges [15], inducing an increase in the wall–pressure fluctuations over the serrations. The latter is associated with the noise increase from serrated trailing edges at high angles, as shown in [10,19].

The modification of the wall–pressure fluctuations for serrated trailing edges is often described as the main cause of the departure between the predicted and the observed noise reduction spectrum from serrated trailing edges [6,18,10]. For example, while models predict an asymptotic noise reduction at high frequencies, experiments and numerical simulations have always demonstrated a cut–off of the noise reduction and even noise increase at high frequencies based on the flow speed (U_∞), and boundary–layer thick-

* Corresponding author.

ness (δ) ($> \frac{U_\infty}{\delta}$) [13,10–12]. Also, analytical models suggest that the higher the serration aspect ratio ($2h/\lambda$) the lower the noise from the serrated trailing–edge. However, Ref. [20] has shown a limit on the serration aspect ratio, where increasing its height ($2h$) or decreasing its wavelength (λ) does not improve the maximum noise reduction and an increase of the high–frequency noise is observed. Ref. [20] has come to the conclusion that, differently from the analytical predictions [4], noise reduction from serrations is more correlated to the ratio $2h/\delta$, and that the aspect ratio ($2h/\lambda$) does not affect noise reduction in the same way as the predictions suggest.

Besides, several serration concepts exist, such as the sawtooth serrations, the concave–shaped (iron, or ogee–shaped) serrations [11,21], and the combed–sawtooth serrations [2]. Despite that, there is no consensus on the advantages and disadvantages of each geometry, which is also dependent on airfoil geometry, flow conditions, and installation effects. Therefore, the design of trailing–edge serrations lack general guidelines and still requires dedicated numerical simulations and experimental campaigns for each application.

In this work, design guidelines for trailing–edge serrations are sought. To create these guidelines, a parametric study based on experiments with sawtooth serrations of different scales and other geometries, namely concave–shaped, and combed–sawtooth serrations is carried out. Differently from other parametric studies [20,22,23], this work proposes a sensitivity–based approach, based on a reference sawtooth serration geometry, where each parameter of this serration design that affects the trailing–edge noise is varied separately. The trends found are interpreted through the physical mechanisms described in previous research. The model of a benchmark airfoil section [24], the NACA 63$_3$–018, is selected for the experiments and tested under different conditions of flow speeds and angles of attack to build a complete picture of the acoustic properties of serrated trailing edges. A description of those experiments is presented in Section 2 including flow conditions, serration geometries, acoustic measurements, and post–processing techniques. Section 3 reviews the physics of noise scattering from serrated trailing edges and of the wall–pressure fluctuations on the serration surface, which is used in the results section of the work (Section 4) to interpret the results obtained. Design guidelines and conclusions are shown in Sections 5, and 6 respectively.

2. Experimental methodology

2.1. Flow facility, model, and flow conditions

Experiments are conducted in the aeroacoustic wind–tunnel facility at the Delft University of Technology (A-Tunnel). The open test section wind tunnel has an option of exchanging nozzles that allows controlling maximum speed and model dimensions. In this campaign, a rectangular 0.4×0.7 m nozzle is selected, resulting in a maximum flow speed of 35 m/s. The test section is enclosed by an anechoic chamber where the acoustic measurements are carried out. The chamber is designed to avoid reflections from frequencies higher than 150 Hz. More details about the facility are shown in [25].

The model used is a symmetric 2D NACA 63$_3$–018 airfoil with 0.2 m chord and 0.4 m span. This airfoil is chosen following the efforts to create facility-validated benchmark data [24]. The model symmetry allows for assessing the radiated noise from the trailing edge without aerodynamic loading conditions on the serrations (airfoil at $\alpha = 0°$) and comparing it with conditions with aerodynamic loading. Besides, the low trailing–edge angle (δ_{TE}) of less than 4° is appropriate to reduce installation effects in the wedge junction between the serration and the airfoil trailing edge. The trailing edge section is separated at 80%c to allow the installation

of different inserts. An insert with the baseline airfoil trailing-edge is used as the reference configuration while an insert with two claps is used to allow the serrated trailing–edges to be placed. The baseline insert has a trailing–edge thickness of about 0.15 mm, while the serrated trailing–edges inserts are 1 mm thick. The serrations have their centre aligned with the baseline trailing–edge location and are manufactured via laser cutting of a steel sheet. Fig. 1 shows a schematic of the setup and the model installed in the wind–tunnel facility.

A zig–zag tripping tape of 0.6 mm height is placed at 5%c on both sides of the model to force the laminar–to–turbulent transition location at all tested conditions, following the benchmark work of Ref. [24]. For most of the analyses, the model is tested at three different flow speeds (15,20, and 30 m/s). Measurements are taken at angles of attack (α) from 0° to 10° in steps of 1°, and from 10° to 20° in steps of 2°. To measure the acoustic emissions from both the suction and the pressure sides, the measurements are carried out for positive and negative angles of attack. Table 1 summarizes the conditions of test.

A pitot rake is installed at the model to measure the boundary-layer properties at the trailing–edge region. The rake contains 12 total pressure tubes along the wall-normal direction and 2 static tubes on each side of the model (upper and lower side). The measurements are used to assess the boundary-layer velocity profile at mid-span and 90%c location for the reference configuration. The effect of the tubes in proximity to the airfoil walls is corrected following the work of [26]. Fig. 2a shows the setup of the measurement and Fig. 2b the resulting boundary–layer displacement thickness from the experiment. The displacement thickness is used in the remainder of this work to characterize the acoustic emissions at the trailing edge.

2.2. Serration geometries

The serrations are varied by modifying their scaling (height, and wavelength for the sawtooth design), geometry (for the sawtooth vs. concave–shaped serrations), and comb size (for the combed–sawtooth serrations). A reference serration is defined with a height $2h = 30$ mm, and a wavelength $\lambda = 15$ mm ($2h/\lambda = 2$). The reference serration dimension follows Ref. [10], which has demonstrated adequate noise reduction levels for serrations with $2h/\delta \approx 4$ (δ based on the $\alpha = 0°$ condition), and $2h/\lambda = 2$. The other geometries are built upon variations of the reference geometry, creating a sensitivity–based study using a one–factor–at–a–time approach.

Table 2 shows the designs used for the study of the geometric scaling of the sawtooth serrations. For the analyses, three parameters are chosen, namely the serration height ($2h$), wavelength (λ), and aspect ratio ($2h/\lambda$). For each of the parameters, 4 serrations exist where its value remains the same while the other parameters are changed individually. Following this approach, 4 geometries have the same height ($2h = 30$ mm) but different wavelengths and aspect ratios, other 4 have the same wavelength ($\lambda = 15$ mm) but different heights and aspect ratios, and other 4 have the same aspect ratio ($2h/\lambda = 2$) but different heights and wavelengths.

The geometric changes are based on the concave–shaped serrations (ogee–shaped serrations) described in Refs. of [11,21]. The geometries are generated following Eq. 1. In the equation, the parameter n controls the geometry of the serration, $n = 1$ yields the sawtooth design. If $n < 1$, the serration presents a concave shape, i.e. the angles at the root are higher than at the tip. If $n > 1$, the serration presents a convex shape with angles at the tip higher than the ones at the root. In turn, n is controlled based on the desired percentage of surface area compared to the total area of the trailing edge, referred to in this work as the solidity factor (*SF*), following Eq. 2. Similarly to the previous study, 4 different geometries are se-
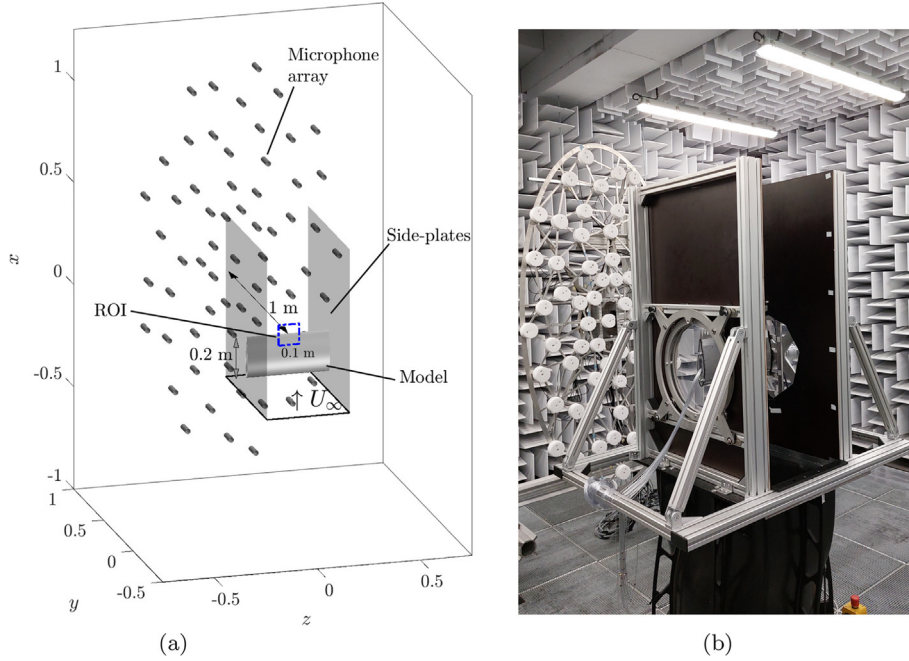
Fig. 1. Experimental setup for acoustic measurements. (a) Schematic of the experiment, and (b) picture of the model mounted in the wind–tunnel facility.

Table 1
Flow conditions selected and available dataset of the acoustic campaign carried out.

U_∞ [m/s]	Re_c	α [°]
15	200,000	[−20:2:−12 −10:1:10 12:2:20]
20	270,000	[−20:2:−12 −10:1:10 12:2:20]
30	400,000	[−20:2:−12 −10:1:10 12:2:20]

lected, with solidity factors of 0.2 (convex–sawtooth serrations), 0.5 (reference sawtooth serrations), 0.7, and 0.8 (concave–sawtooth serrations). Table 3 shows the geometries selected.

$$x(z) = \begin{cases} 2h\left(\frac{2z}{\lambda} + 1\right)^n, & -\frac{\lambda}{2} \leqslant x \leqslant 0 \\ 2h\left(-\frac{2z}{\lambda} + 1\right)^n, & 0 < x \leqslant \frac{\lambda}{2} \end{cases} \tag{1}$$

$$SF = \frac{\int_{-\lambda/2}^{\lambda/2} x\,dz}{2h\lambda} = \frac{1}{n+1}. \tag{2}$$

For the combed sawtooth design, two parameters are selected, namely the number of combs per wavelength (N_{teeth}), and the ratio between the comb pitch and the open pitch. The latter affects the solidity factor (SF) more significantly and is described using the same parameter. Geometries are created for each of the two parameters as shown in Tables 4 and 5. It is important to highlight that the combed–sawtooth designs corresponding to $N_{\text{teeth}} = 5$ in Table 4, and $SF = 0.75$ in Table 5 are the same.

2.3. Acoustic measurement technique and post processing

The noise levels of the serration designs are assessed through measurements with a microphone array. The schematic in Fig. 1a shows the setup for the acoustic measurements. The microphone array used consists of 64 G.R.A.S. 40PH microphones connected to a PXIe system with 4 PXIe-4499 acquisition boards. Details of the apparatus and data acquisition parameters are reported in Table 6.
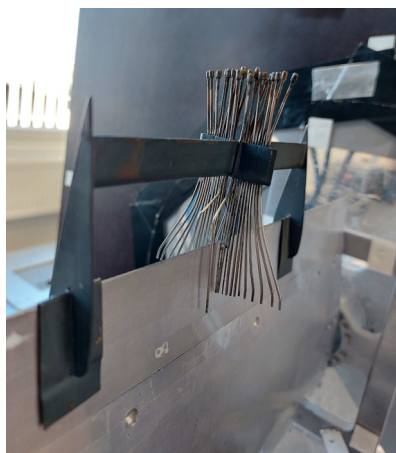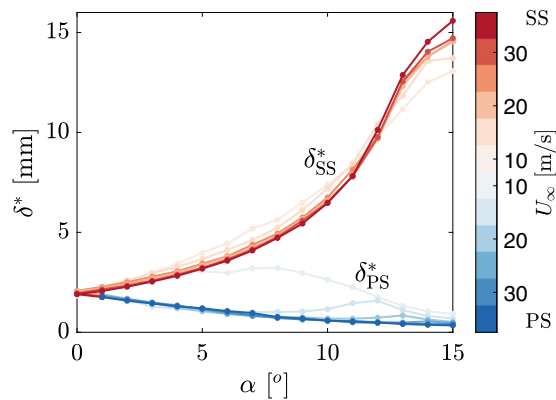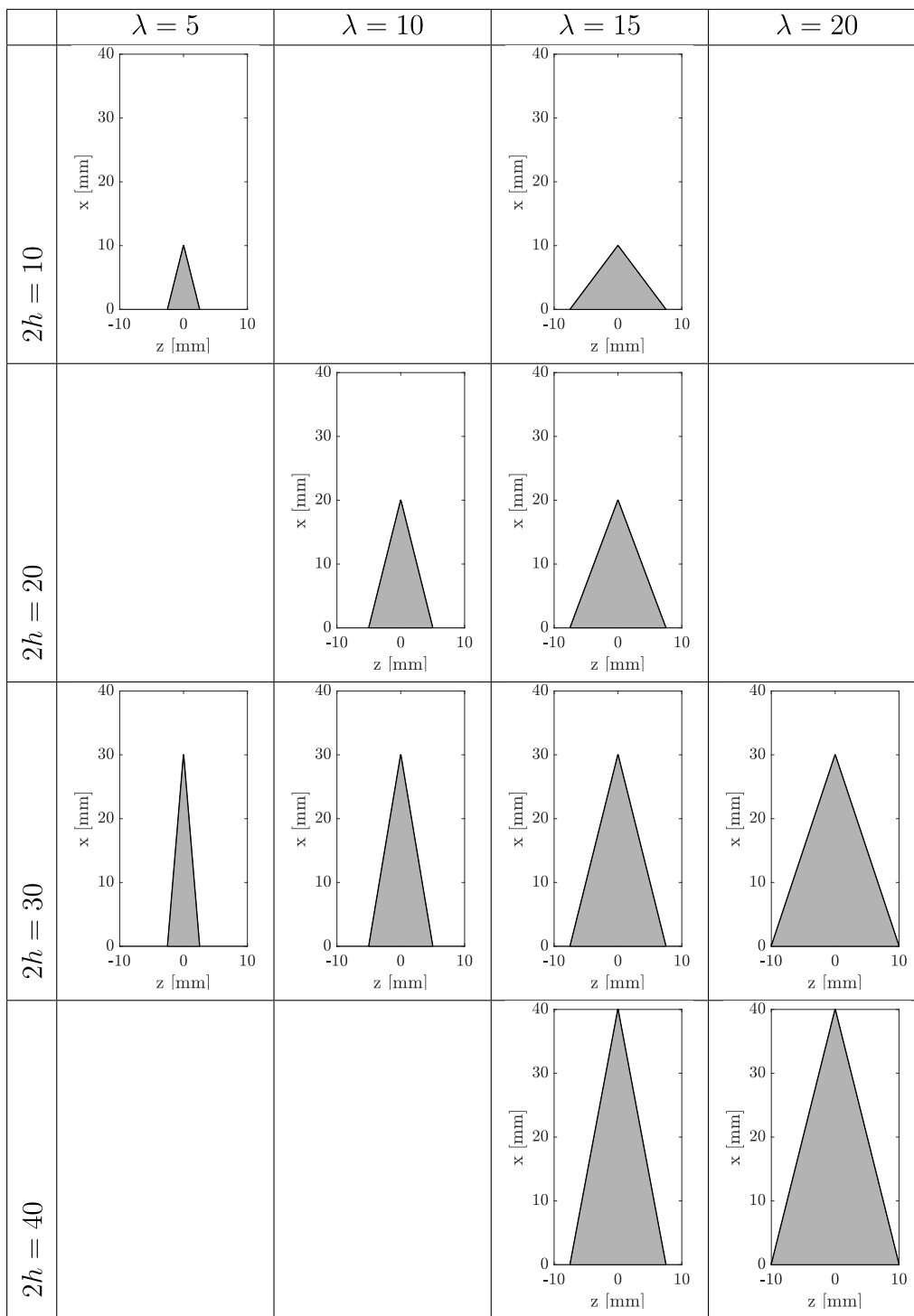

Fig. 2. Experimental setup of the pitot–rake (a), and measured boundary–layer displacement thickness (b).
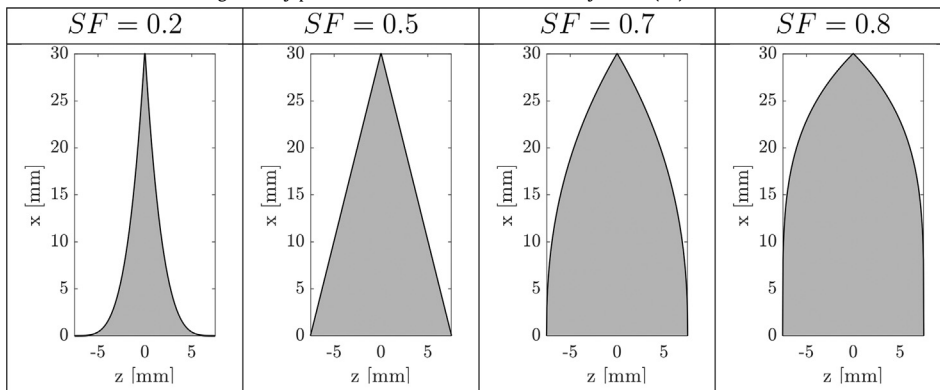
Table 2

Geometry of the sawtooth serrations selected for the scaling study of trailing-edge serrations. Dimensions are shown in millimeters.

The data acquired are processed with the conventional beam-forming technique described in Ref. [27]. The steering vector formulation number I from Ref. [28] is selected and the effect of the flow velocity is corrected following the simplification proposed in Ref. [27]. Resulting source maps of the baseline serration are shown in Ref. [24]. The trailing-edge sources can be observed for frequencies from 400 to 5,000 Hz.

To better isolate the noise from the trailing edge, a source power integration (SPI) procedure is used. Sources on the mid-span of the trailing edge are integrated inside a region of 100×100 mm^2 ($0.5c \times 0.5c$). For conditions under angles of attack, the spectra presented are averaged from the results taken from both the pressure and suction side, following the procedure discussed in Ref. [29]. Fig. 3 shows the difference between the noise levels of the baseline

Table 3
Concave vs. convex serration geometry parametrization based on the solidity factor (*SF*).

$SF = 0.2$	$SF = 0.5$	$SF = 0.7$	$SF = 0.8$

Table 4
Combed–sawtooth geometric parametrization based on the number of combs per wavelength (N_{teeth}).
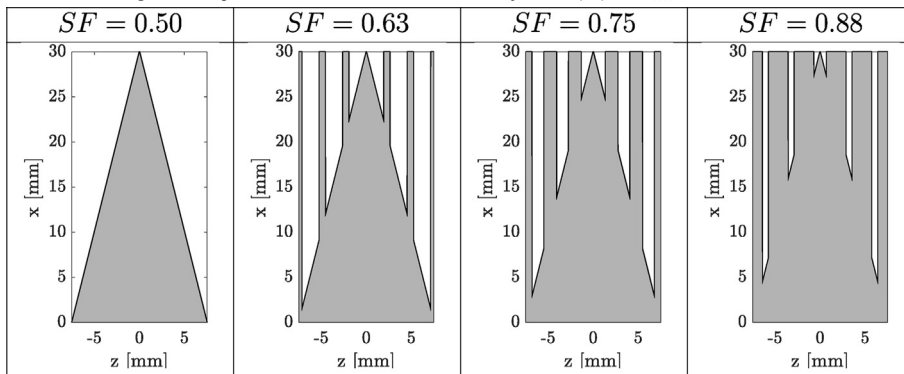
$N_{\text{teeth}} = 0$	$N_{\text{teeth}} = 1$	$N_{\text{teeth}} = 3$	$N_{\text{teeth}} = 5$	$N_{\text{teeth}} = 7$
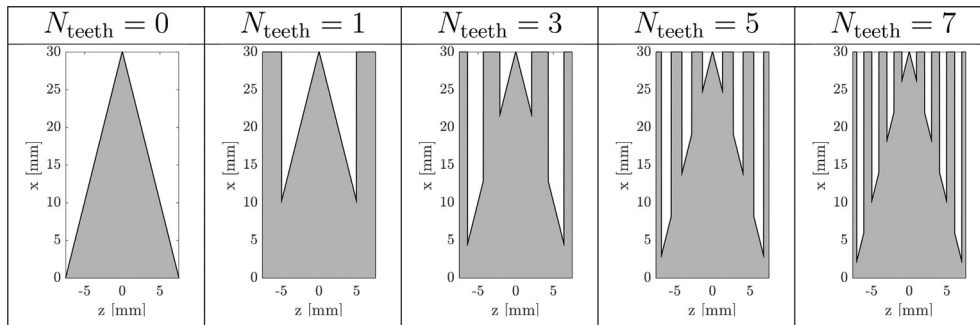
Table 5
Combed–sawtooth geometric parametrization based on the solidity factor (*SF*) for $N_{\text{teeth}} = 5$.

$SF = 0.50$	$SF = 0.63$	$SF = 0.75$	$SF = 0.88$

Table 6
Setup of the acoustic array measurement and acquisition system.

Number of microphones	64
Microphone type	G.R.A.S. 40PH
Frequency range	50 Hz to 20 kHz
Acquisition system	NI PXIe
Acquisition board	PXIe-4499 (x4)
Voltage range	±10 V
ADC converter precision	24 bits
Array *x*-span	2.0 m
Array *y*-span	1.0 m

airfoil and the same measurements carried out for the test section without the model, taken here as the reference background noise. All spectra are presented in twelfth-octave bands. Negative values indicate that the background noise is lower than the baseline noise of the airfoil (black line in the graph). The black line represents the noise reduction floor for the measurements. Measurements of serrations that would reduce more noise than the background levels are compromised due to the background noise. In the same figure, the noise reduction obtained with the reference serration geometry is shown in blue. The results show that the noise levels from the serrated trailing edge are still 2–3 dB above the background ones, indicating that the measurements are not hampered or affected by the facility background levels within the frequency range of interest.
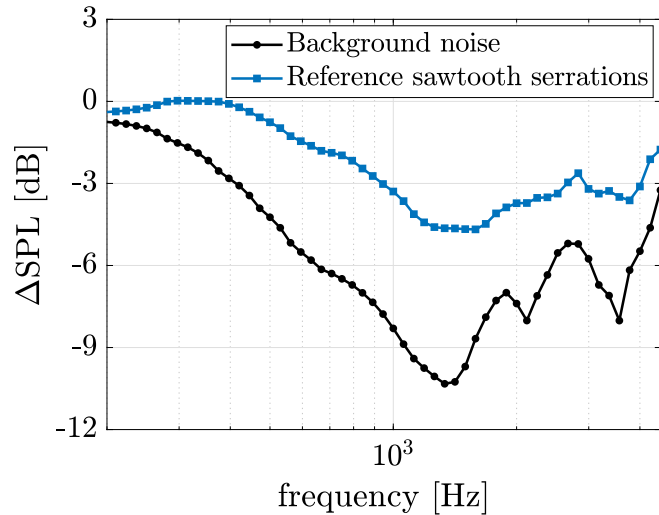
Fig. 3. Measured difference between background noise and baseline noise levels (black curve) obtained with source power integration from the centre span region. The difference between the reference sawtooth serration design and the baseline noise levels is shown in blue. Negative values of ΔSPL indicate noise reduction. Background noise measurements are obtained by removing the model from the test section while measuring at the same flow speed.
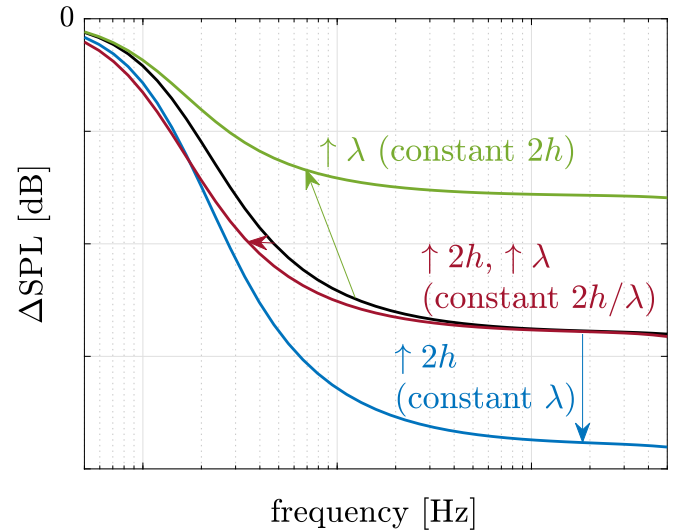

Fig. 4. Example predicted variation of the noise reduction depending on the serration dimensions. The predictions are obtained with the rapid method from Lyu and Ayton 2020 [8]. The black line represents the reference noise reduction while the other lines illustrate the effect of different modifications of the serration geometry. Negative values of ΔSPL indicate noise reduction.

3. A review on the analytical description of acoustic scattering and wall–pressure fluctuations on serrated trailing edges

Understanding the driving parameters of serration design requires knowledge of the effects of each geometric modification on the acoustic scattering and the flow field at the trailing edge. This section gives a review of the main conclusions from the literature concerning serration acoustic scattering and modification of the wall–pressure fluctuations around the serration design. The concepts described in this section are used to guide the discussions of the results in Section 4.

3.1. Acoustic scattering

Refs. [5–7] have described the scattering of the incoming turbulent wall–pressure fluctuations on the trailing edge of a semi–infinite plate, creating models that predict the noise reduction obtained by trailing–edge serrations. These models depend on the incoming wall–pressure wavenumber spectrum over the serration, assumed to be invariant to the position along the serration. These different models have common conclusions concerning the serration design. For example, all models predict that the noise reduction obtained from the serrations reaches an asymptotic value at high frequencies [5–7], as demonstrated in Fig. 4. The figure is obtained with the rapid model described in Ref. [8].

The simplified model of Ref. [5] brings important insights into the characteristics of the noise reduction spectrum obtained from a serrated trailing edge. According to the work, the noise reduction reaches an asymptotic value described by Eq. 3. The limit is valid for high frequencies ($\frac{f\delta}{U} \gg 1$) and high serrations aspect ratios ($\frac{2h}{\lambda}$). Similar assumptions can be used to derive an equation for the cut-on frequency, i.e. the frequency where the noise reduction reaches half (−3 dB) of its asymptotic value. This procedure yields Eq. 4, in which the cut-on frequency ($f_{\text{cut−on}}$) depends only on the flow speed and the serration wavelength. Still, it is important to point out that the model of Howe has shown a significant overestimation of the noise reduction obtained, as demonstrated in the works of Refs. [13,10].

$$\Delta \text{SPL}_{\text{max}} = \log \left[1 + 4 \left(\frac{2h}{\lambda} \right)^2 \right]. \tag{3}$$

$$f_{\text{cut−on}} = \frac{2}{\pi} \frac{U_c}{\lambda}. \tag{4}$$

Effect of varying the serration height (constant λ): Following Refs. [5,21], increasing the serration aspect ratio ($2h/\lambda$) yields an improvement of the asymptotic noise reduction from the serrations (as depicted in Eq. 3). Also, according to the scattering models, changes in the serration height do not affect the frequency range where noise reduction happens (Eq. 4). This is shown in the blue line of Fig. 4 where the modification of the height only modifies the asymptotic predicted value of the noise reduction, without altering the frequency in which this value starts.

Effect of varying the serration wavelength (constant 2h): Similar to the serration height, analytical scattering models predict that, by decreasing the serration wavelength, a higher asymptotic level of noise reduction is expected [21]. However, the serration wavelength influences the frequency at which the noise reduction reaches its asymptotic value, following Eq. 4. Therefore, the analytical methods suggest that the higher the serration wavelength, the lower the noise reduction obtained is but also the lower the frequency where noise reduction starts, as illustrated by the green line in Fig. 4.

Effect of varying the serration scale (constant 2h/λ): The serration scale defines the frequency range where noise reduction starts. By increasing the serration height (2h), and wavelength (λ) while keeping 2h/λ constant, the noise reduction is not expected to change but the frequency where the asymptotic noise reduction starts is lowered. This is illustrated by the red line in Fig. 4, and indicates that the scaling of the serration can be tuned according to the desired frequency of noise reduction.

3.2. Wall–pressure fluctuations along the serration surface

The models mentioned previously are based on a wavenumber–frequency spectral representation of the wall–pressure fluctuations beneath a turbulent boundary layer. This representation considers

pure convection (Taylor's frozen turbulence assumption [30]) along the serration surface.

However, studies [31,16,11,12] have demonstrated that the wall–pressure fluctuations vary along the trailing–edge serrations. Ref. [17] has described three physical mechanisms that affect the wall–pressure fluctuations along the serration surface. These mechanisms affect directly the scattering levels, in turn modifying the noise reduction obtained. Ref. [11] has shown that the scattering is more intense in the regions where the wall–pressure fluctuations are higher. Ref. [32] demonstrated good predictions of the serration noise reduction when using the simulated wall–pressure fluctuation close to the serration. All these works highlight the importance of considering how the wall–pressure fluctuations vary with the serration geometry on the prediction of trailing–edge noise. Therefore, this section briefly describes the physical properties observed for the wall–pressure fluctuations on the surface of serrated trailing edges according to [17] and how they may affect the scattered noise. Fig. 5 illustrates how these three mechanisms affect the distribution of the wall–pressure fluctuations on the serration surface.

Impedance change at the trailing edge: As the flow passes from a solid boundary to an open region at the trailing edge, the pressure fluctuations along the plane of the airfoil chord are reduced. Ref. [17] has shown that this modification causes the wall-pressure fluctuations to reduce progressively from the root to the tip of the serrations. This effect is especially pronounced at low frequencies, where the turbulent scales are larger and the transition effect is distributed over the serration surface. Fig. 5 shows the effect of the impedance transition on the distribution of the wall–pressure fluctuations over the serration surface. As shown, the wall–pressure fluctuations are higher at the serration root and lower at the

serration tip, indicating that scattering, at low frequencies, is more intense at the serration root, as discussed in the work of [11]. In turn, the latter work has suggested that concave–shaped serrations perform better at low frequencies as the geometry poses a higher serration angle at the root, where the fluctuations are higher, consequently reducing the scattered noise.

Wake development and acceleration of turbulent structures: As the flow develops along the open region on the serrations, the small scales of turbulence are accelerated throughout the serration gap, eventually impacting the speed at which they are convected. Ref. [17] demonstrates that this acceleration causes the amplitude of the wall–pressure fluctuations around the tip of the serrations to increase, as shown in Fig. 5. Since this acceleration happens mainly for the inner scales of turbulence, the frequency where this effect is observed can be estimated by Eq. 5, following Ref. [33] where u_τ is the boundary–layer friction velocity, and v the flow kinematic viscosity. Ref. [11] also demonstrates that this increase is associated with a more intense scattering at high frequencies along the tip of the serrations. The latter causes the noise reduction to reduce at high frequency, in turn causing the cut–off of the noise reduction, not predicted by the analytical scattering methods.

$$f_{\text{cut-off}} \approx 0.05 \frac{u_\tau^2}{v}. \tag{5}$$

Aerodynamic loading effect: This effect is only existing when serrations are placed at an angle with respect to the flow direction, and aerodynamic loading is created over the serration surface. It relates to the wall–pressure fluctuations due to the secondary flow accelerations generated along the serration edge. According to Ref. [17], the vortex pairs formed around the serration edges under loading [15] are responsible for an extra broadband component to the wall–pressure spectrum that is proportional to the serration aspect ratio ($2h/\lambda$), and is maximum at a Strouhal number that can be described by Eq. 6. Ref. [12] has shown that by adding combs to the serration (combed–sawtooth design), the secondary flow accelerations are greatly suppressed, yielding improved noise characteristics.

In this work, these secondary flow features are created by placing the airfoil at different angles of attack. This is done so as the symmetric airfoil with serrations aligned with the chord line allows for a controlled aerodynamic loading condition. In practice, the aerodynamic loading is generated not only due to the angle of attack but also due to the asymmetry of the airfoil selected [20], and the installation angle of the serrations [34,35]. Ref. [12] has also demonstrated that similar secondary flow formations are observed for airfoils with thick trailing–edge angles. In the latter, a NACA 0018 equipped with trailing–edge serrations is tested. In this setup, the installation of the serrations aligned with the chord line creates a wedge angle of about 12° between the airfoil trailing edge and the serration plane.

$$\frac{f_{\text{load}}\delta^*}{U_\infty} = \frac{1}{4}\frac{\delta^*}{2h} + \frac{\sqrt{\pi}}{5}. \tag{6}$$

4. Results and discussions

In this section, the results of the acoustic measurements are discussed. The first subsection is dedicated to the basic features of the noise reduction from serrated trailing edges. The influence of flow conditions such as the flow speed and angle of attack is discussed. The second subsection is dedicated to the scaling of sawtooth trailing–edge serrations, i.e. the influence of parameters such as the serration height ($2h$), wavelength (λ), and aspect ratio ($2h/\lambda$). The third section describes the modifications of serration geometry in terms of concave and convex–shaped serrations while the last
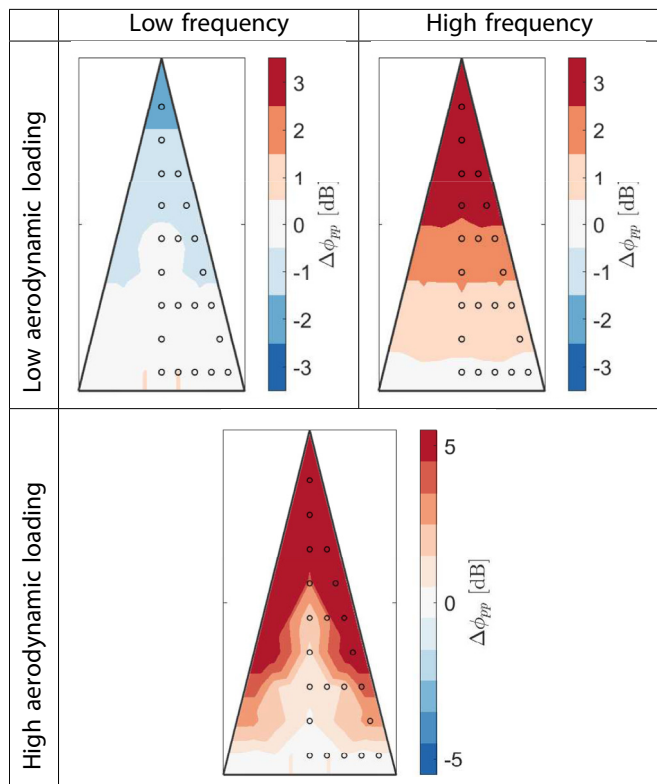
Fig. 5. Exemplified distribution of the wall–pressure fluctuations over a serrated trailing edge under different conditions as described in Ref. [17]. Reference wall–pressure spectrum level ($\Delta\phi_{pp} = 0$) is set at the centre and root of the serration. Data is taken from measurements with the same airfoil at $\alpha = 0^o$ (low aerodynamic loading) and $\alpha = 10^o$ (high aerodynamic loadin at a Reynolds number of 1×10^6.

one is dedicated to the effect of introducing combs on the sawtooth serration.

4.1. General characteristics of trailing–edge serration noise

This section gives a description of the noise reduction obtained from serrated trailing edges. The acoustic results shown in this section describe the noise reduction spectrum of the reference serration design ($2h = 30$ mm, and $\lambda = 15$ mm) and how it varies with the different flow conditions tested.

At first, the variation of the noise reduction with the flow speed is assessed, as shown in Fig. 6. In Fig. 6(a), the dimensional frequencies demonstrate how the noise reduction created by the serrations is shifted from lower frequencies at low speeds to higher ones at high speeds. Following previous works [11,12,20,36], the measured noise reduction from serrated trailing–edges starts at a certain frequency, reaches a maximum, and decays for higher frequencies.

In Fig. 6(b), the spectrum of the noise reduction is scaled with the Strouhal number based on the boundary–layer displacement thickness of the baseline airfoil (δ^*) and the flow speed. Apart from a minor modification of the amplitude of the maximum noise reduction, the collapse of the curves demonstrates how the choice of Strouhal number is a valid one to describe the spectrum of noise reduction of a certain serration design. This property has already been shown in Refs. [20,24]. Discrepancies are observed at high frequencies and are believed to be related to the different proportionality of the high–frequency cut–off due to the wake acceleration effects. Following Eq. 5, the scaling of the wake acceleration with the Strouhal number based on the flow viscosity and friction velocity ($f\nu/u_\tau^2$) creates modifications on the non-dimensional spectral shape between different speeds.

The non-dimensional spectrum shape is expected to vary for different serration geometries. Nevertheless, results and literature [20] have consistently shown that maximum noise reduction is observed around a Strouhal number 0.09, following Eq. 7. This Strouhal number coincides with the one of maximum trailing–edge noise according to Ref. [37]. According to the figure, the noise reduction starts at a Strouhal number of about 0.03 and decays monotonically after the Strouhal number of maximum noise reduction.

$$f_{\max} = 0.09 \frac{U_\infty}{\delta^*}. \tag{7}$$

The choice of the boundary–layer displacement thickness for the Strouhal number normalization is more complicated under asymmetric flow conditions, i.e. angles of attack different than 0° or for the flow over asymmetric airfoils. As discussed in Ref. [37], the thick boundary layer on the suction side is responsible for the noise generated at lower frequencies whereas the thin boundary layer on the pressure side is responsible for the noise at higher frequencies. These differences are explored in Fig. 7(a) which shows how the noise reduction is modified for different angles of attack. Results show that the noise reduction is primarily shifted towards a lower frequency range, indicating that the noise reduction from the suction side is predominant. Nevertheless, as a simplified rule of thumb, this noise reduction can be normalized by the averaged boundary–layer thickness, i.e. $\delta^*_{AV} = \frac{1}{2}\left(\delta^*_{SS} + \delta^*_{PS}\right)$, where δ^*_{SS} is the boundary–layer displacement thickness at the suction side and δ^*_{PS} at the pressure side. Results from the Strouhal scaling are shown in Fig. 7(b), which produces a fairly good agreement, especially at low Strouhal numbers and small angles of attack.

The non-dimensionalized spectra also show the effects associated with the aerodynamic loading of the serrations at high angles of attack. The aerodynamic loading causes an increase in the noise from the serrations, hampering the noise reduction achieved at high frequencies. This increase of noise is noticeable for angles higher than 8° at a Strouhal number of about 0.40. The value is similar to the one obtained with Eq. 6 of 0.41 for the Strouhal of maximum increase of the wall-pressure fluctuations due to aerodynamic loading. The value is shown in Fig. 7(b) by the black dashed line in the figure.

4.2. Sawtooth serration scaling

4.2.1. Dependence on the serration height (constant $\lambda = 15$ mm)

In this section, the effect of increasing the serration height while keeping its wavelength fixed ($\lambda = 15$ mm) is studied. Four different serration heights are tested and the resulting noise reduction spectrum is shown in Fig. 8(a) for $\alpha = 0°$, where $\delta^* = 2.1$ mm, and 8(b) for $\alpha = 10°$, where $\delta^* = 4.2$ mm (average). These angles are selected because $\alpha = 0°$ represents a condition without aerodynamic loading while $\alpha = 10°$ is a representative high aerodynamic

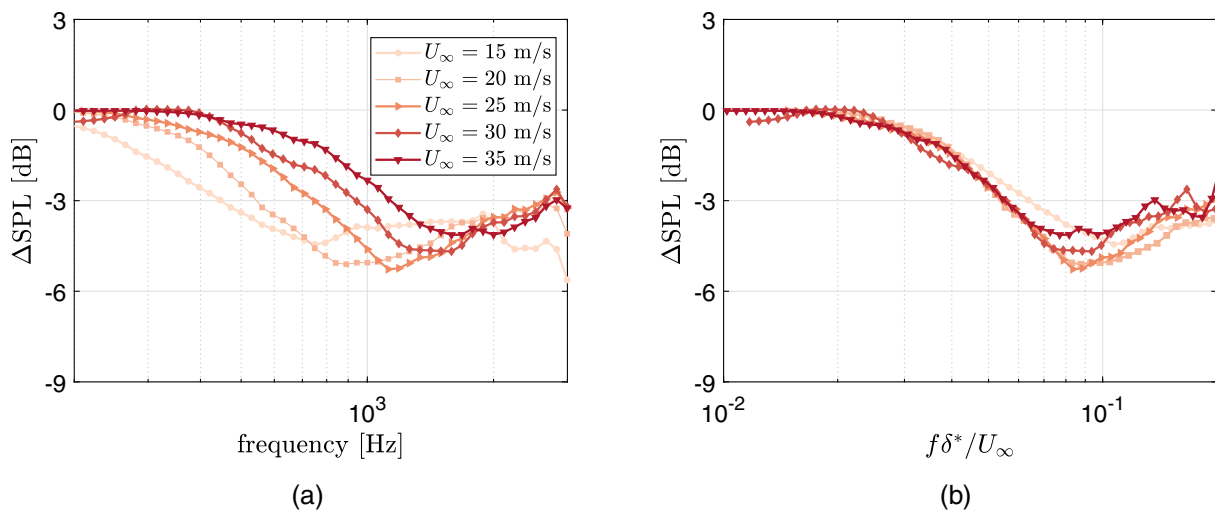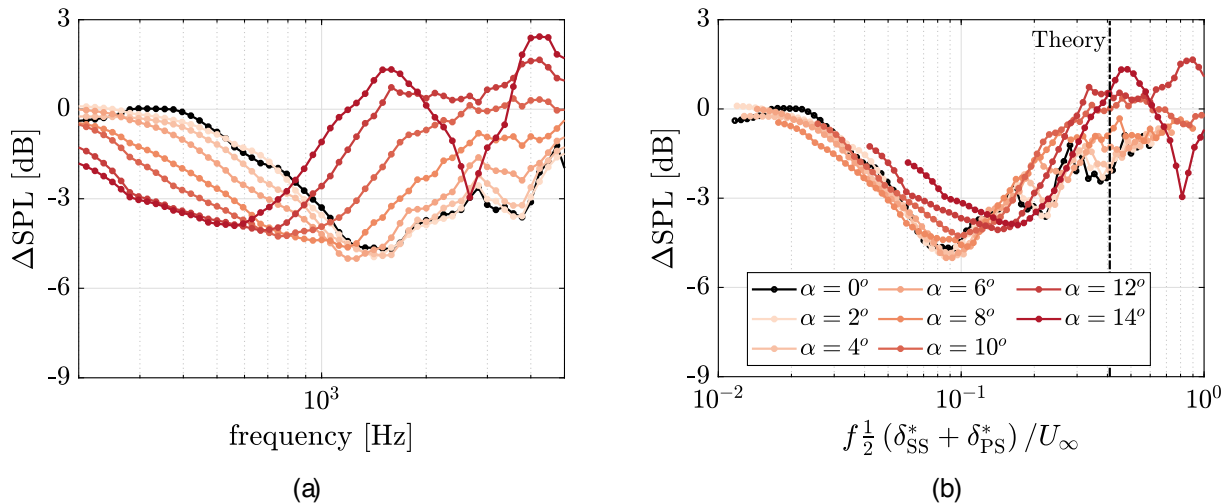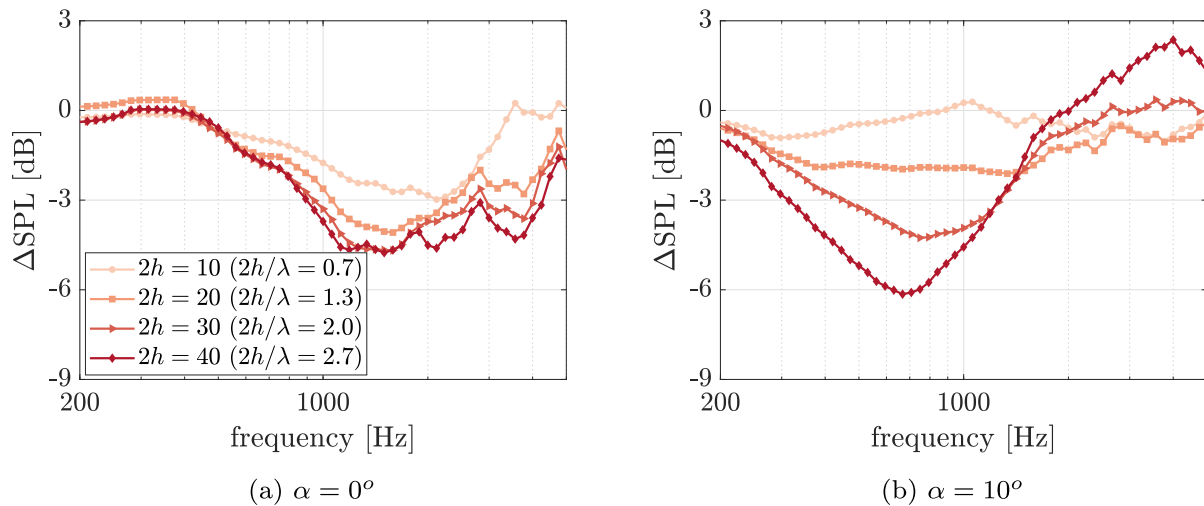**Fig. 6.** Measured noise reduction (ΔSPL) obtained at different flow speeds at $\alpha = 0°$. Figure (a) shows the noise reduction measured against the dimensional frequency, and (b) shows the noise reduction versus the non-dimensional frequency obtained using the boundary-layer displacement thickness. The results are obtained for the serration of $2h = 30$ mm, $\lambda = 15$ mm, and $2h/\lambda = 2$.

Fig. 7. Measured noise reduction (ΔSPL) obtained at $U_\infty = 30$ m/s at various angles of attacks. Figure (a) shows the noise reduction measured against the dimensional frequency, and (b) shows the noise reduction versus the non-dimensional frequency obtained using the average boundary-layer displacement thickness. The black–dashed line represents the Strouhal number where the increase of wall-pressure fluctuations due to aerodynamic loading is maximum, according to Eq. 6.

Fig. 8. Measured noise reduction (ΔSPL) obtained at $U_\infty = 30$ m/s by varying $2h$ while keeping λ constant. (a) $\alpha = 0^o$ ($\lambda/\delta^* = 7.1$), and (b) $\alpha = 10^o$ ($\lambda/\delta^* = 3.5$).

loading case, where no separation is observed at the trailing edge from the pitot–rake measurements.

From the $\alpha = 0°$ condition (Fig. 8a), it is clear that the higher $2h$ translates to a higher noise reduction as predicted. Nevertheless, the expected improvement of the noise reduction is limited for serration heights above $2h \gtrsim 12\delta^*$ ($2h \gtrsim 2\delta$). In the figure, the highest serrations ($2h = 30$, and $2h = 40$) yield similar levels of noise reduction, indicating that increasing the height above this limit does not yield any further improvement. This result is also observed in Ref. [20], where the gain in noise reduction between the two serration heights tested is small for conditions where $2h/\delta^* > 8$. The results are opposite to the predictions from theory [5,18], where the increasing serration height always yields an improvement of the noise reduction. Following Ref. [17], the increase of the serration height is supposed to accentuate the wake acceleration effects, thus intensifying the increase of noise from the serrations at high frequencies. It is believed that this effect is the underlying cause of the observed upper limit for the serration height.

Fig. 8(a) also shows that the noise reduction starts approximately in the same frequency range. The results agree with the

scattering prediction models [5], as the increasing height does not impact the cut–on frequency (Eq. 4).

The effect of modifying the serration height under different angles of attack is seen in Fig. 8(b), where the small $2h$ serrations present lower noise reduction at low frequencies and higher noise reduction at high frequencies compared to large serrations. The serration of $2h = 40$ mm even demonstrates a noise increase in the order of 3 dB against a straight trailing edge at high frequencies.

According to the theory, the increasing height modifies the sensitivity to the angles of attack. Following Ref. [17], the increasing height decreases the frequency where aerodynamic loading affects the noise from serrations and increases its associated wall–pressure fluctuations. The results indicate that a higher serration experiences a stronger loss of noise reduction when at an angle than a short one. This means that increasing the serration height beyond the necessary ($2h/\delta^* \gg 12$) does not bring a meaningful increase in the maximum noise reduction and creates a design that is more sensitive to changes in flow conditions, e.g. variations of the angle of attack during the operation.
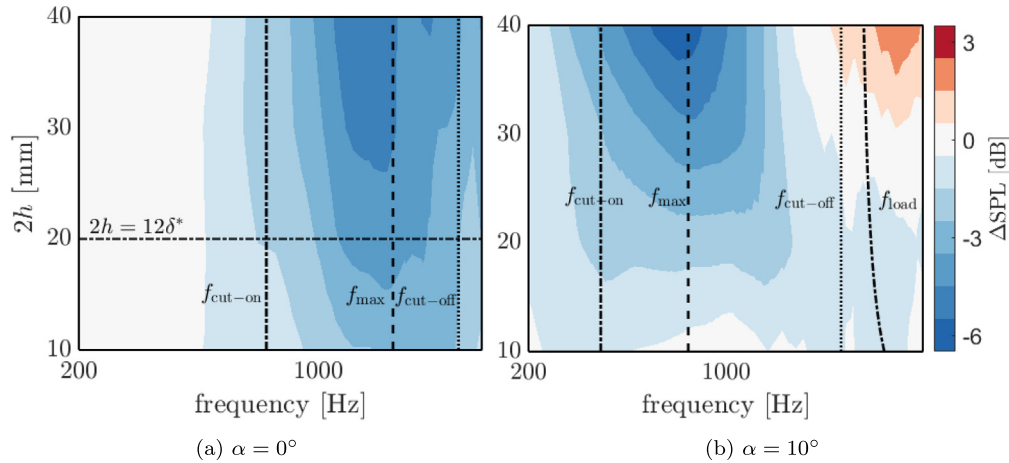
Fig. 9. Contour plot of the variation of noise reduction for $\alpha = 0°$ (a), and $\alpha = 10°$ (b) at $U_\infty = 30$ m/s with the variation of serration height while the wavelength is kept constant ($\lambda = 15$ mm, $\lambda/\delta^* = 7.1$, and $\lambda/\delta^* = 3.5$ for a, and b respectively). Black lines show the theoretical predictions for the cut–on, max, cut–off, and loading noise frequencies.

Nevertheless, following the criteria for serration height ($2h \gtrsim 12\delta^*$), the thicker boundary layer on the suction side indicates that bigger serration heights are preferable at high angles of attack. The results show that the highest serration ($2h = 40$ mm) is significantly more effective to reduce noise at low frequencies than the smaller ones at $\alpha = 10°$. For this particular condition, the highest serration tested is the only design closer to the criteria of $2h \sim 12\delta^*$, i.e. $2h \approx 10\delta^*$.

The trends described before can also be observed in the contour plots of Fig. 9. In the figures, the x–axis represents the frequency, and the y–axis the change of serration height. Fig. 9(a) shows the obtained results at $\alpha = 0°$. The black vertical lines represent the cut–on, max, and cut–off frequencies, as described in Eqs. 4, 7, and 5. The horizontal line shows the described limit of $2h = 12\delta^*$. These lines indicate the measured trend from the serrations tested. Noise reduction is 3 dB lower than the maximum around the cut–on frequency ($f_{\text{cut−on}}$), reaches its maximum around f_{max}, and decays for frequencies above $f_{\text{cut−off}}$. At $10°$ angle of attack (Fig. 9b), the same trends are observed. Besides, the presence of aerodynamic loading can be observed by the f_{load} curve (Eq. 6) that describes the frequency where aerodynamic loading causes an increase of the noise from the serrated trailing edges. For this case, the $2h = 12\delta^*$ line is not visible as the thicker boundary layer on the

suction side causes the line to be above the highest serration tested. The increasing boundary–layer thickness causes the frequency of maximum noise reduction to decrease, getting closer to the cut–on frequency.

4.2.2. Dependence on the serration wavelength (constant $2h = 30$ mm)

This analysis focuses on the influence of changing the serration wavelength (λ) while keeping a constant serration height ($2h = 30$ mm). In this case, for each angle of attack the non-dimensional quantity $2h/\delta^*$ is kept constant while the serration wavelength is modified, therefore affecting the serration aspect ratio. The noise reduction at $\alpha = 0°$ is shown in Fig. 10(a) while the one obtained at $\alpha = 10°$ is shown in Fig. 10(b). The overall trends at zero degrees angle of attack show that the higher wavelength yields a lower noise emission and a lower frequency where maximum noise reduction is observed. At $10°$ angle of attack, the noise reduction spectra from all the different serrations have a similar spectral shape.

At symmetric conditions ($\alpha = 0°$), the results disagree with the predictions [5,7], where the increasing wavelength yields less noise reduction (the lower the serration aspect ratio, the lower the noise reduction achieved). The results indicate that a wider ser-
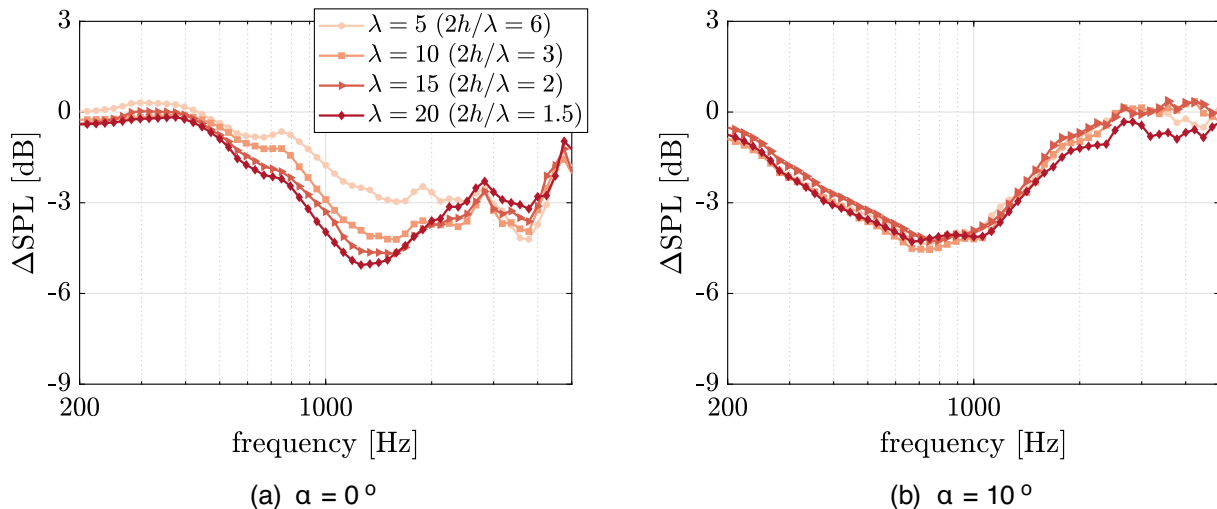
Fig. 10. Measured noise reduction (ΔSPL) obtained at $U_\infty = 30$ m/s by varying λ while keeping $2h$ constant (30 mm). (a) $\alpha = 0°$ ($2h/\delta^* = 14.3$), and (b) $\alpha = 10°$ ($2h/\delta^* = 7.1$).

ration (lower serration aspect ratio) reduces more noise than a narrow one. This behaviour is only observed in the experimental work of [20] for the lowest wavelengths tested. Nevertheless, the predicted modification of the frequency range is observed as the increasing wavelength (λ) yields a shift in the noise reduction towards the lower frequencies, as implied in Eq. 4.

It is here speculated that the lower noise reduction from the narrow serrations is observed due to the small frequency range between the cut–on frequency ($f_{\text{cut–on}}$), the frequency of maximum noise reduction (f_{max}), and the cut–off frequency ($f_{\text{cut–off}}$) for these designs. Following Eqs. 7, and 5, the maximum noise and cut–off frequencies at $\alpha = 0°$ are around 1600, and 2500 Hz respectively. This is observed in Fig. 10(a), as the noise reduction decreases for all the serrations at frequencies above 2000 Hz. However, the cut–on frequency prediction from Eq. 4, tells that the serrations of wavelength 5,10,15, and 20 mm are meant to start reducing noise for frequencies above 2300,1200,800, and 600 Hz respectively. This indicates that the small wavelength designs have a theoretical cut–on frequencies similar to or higher than the predicted frequency where noise reduction is maximum or the one where noise reduction stops. This can be better visualized in Fig. 11(a), where the contour of the variation of the noise reduction spectrum with serration wavelength is shown. The figure also shows the pre-

dicted cut–on, maximum noise, and cut–off frequencies for the different serration wavelengths. These lines follow well the observed trends, i.e. noise reduction is only higher than 3 dB for frequencies above the cut–on frequency, the noise reduction reaches a maximum around f_{max}, and it reduces for frequencies above $f_{\text{cut–off}}$.

Figs. 10(a), and 11(a) indicate that designs where the cut–on, maximum noise, and cut–off frequencies are too close, such as the $\lambda = 5$, and $\lambda = 10$ mm ones, have limited noise reduction. This means that the noise reduction for those designs starts at a frequency close to the ones of maximum noise and of the cut–off frequency, where aerodynamic alterations of the inner scales increase the scattering levels. As a result, the overall achieved noise reduction is significantly reduced. The other two designs show similar noise reduction, although $\lambda = 20$ mm still presents lower noise levels at low frequencies while $\lambda = 15$ mm reduces more noise at high frequencies. By considering that trailing–edge serrations are meant to reduce noise at the regions of maximum noise on a turbulent boundary layer ($f_{\text{cut–on}} < f_{\text{max}}$, in Eqs. 4 and 7). By rearranging the equations and considering $\frac{U_c}{U_\infty} \approx 0.7$, it can be inferred that $\frac{\lambda}{\delta^*} > 5$. This equation represents the first minimum value for the serration wavelength.

At high angles of attack, the improvement of the noise reduction of narrow serrations and the deterioration of the noise reduc-

Fig. 11. Contour plot of the variation of noise reduction for $\alpha = 0°$ (a), and $\alpha = 10°$ (b) at $U_\infty = 30$ m/s with the variation of serration wavelength while the height is kept constant ($2h = 30$ mm, $2h/\delta^* = 14.3$, and $2h/\delta^* = 7.1$ for a, and b respectively). Black lines show the theoretical predictions for the cut–on, max, cut–off, and loading noise frequencies.
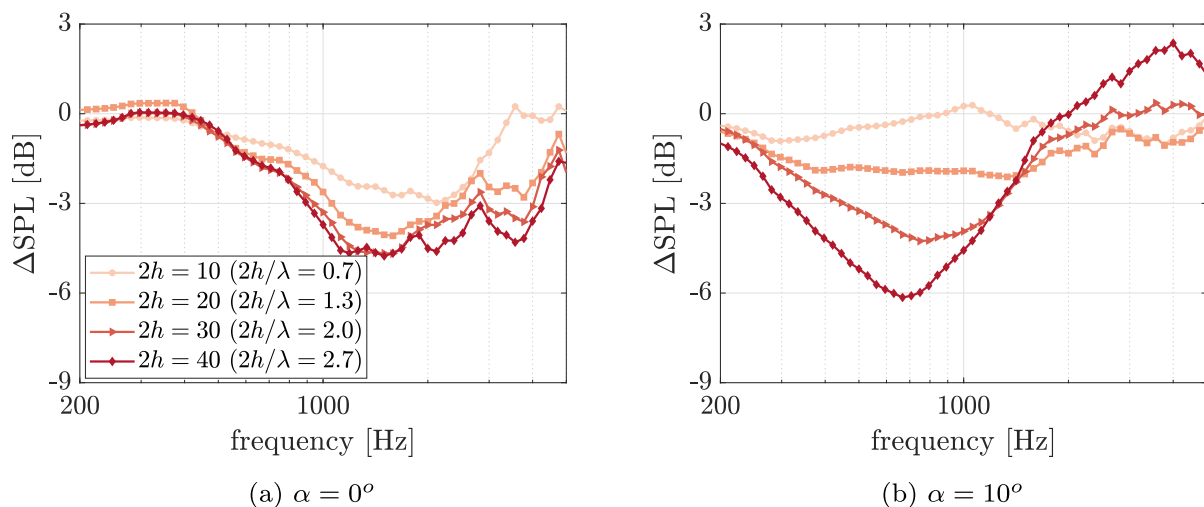
Fig. 12. Measured noise reduction (ΔSPL) obtained at $U_\infty = 30$ m/s by varying $2h$ while keeping λ constant. (a) $\alpha = 0°$, and (b) $\alpha = 10°$.

tion of the wider ones cause all the measured serrations to present a similar noise reduction spectrum. The results indicate that the wider serrations are more affected by the angle of attack change, due to their higher surface area and consequent aerodynamic loading generated. The similar noise reduction performance also suggests that the frequency where the aerodynamic loading affects the serration noise is not modified with the serration wavelength, as predicted by the theory. The latter can be also observed in the contour plot in Fig. 11(b) where the frequency of maximum aerodynamic–loading influence is shown. At this condition, the cut–on frequency does not describe the frequency where noise reduction starts. This behaviour is associated with the small difference between the maximum and cut–on frequencies at such conditions.

4.2.3. Dependence on the serration scale (constant $2h/\lambda = 2$)

The last geometric property of the sawtooth design to be assessed is the scaling of the serration with respect to the incoming turbulent scales, i.e. the consequences of keeping the serration aspect ratio constant ($2h/\lambda = 2$) while modifying both the height and wavelength of the serrations. The resulting noise reduction spectrum is observed in Fig. 12, where Fig. 12(a) shows the results obtained at $\alpha = 0°$, and Fig. 12(b) at $\alpha = 10°$.

From the results at zero angle of attack, the serration scale changes both the maximum noise reduction and the frequency of

maximum noise reduction. According to the analytical scattering models [5], the scaling of the serrations alters only the frequencies where noise reduction starts. However, the experiments show that the cut–on frequency also affects the maximum noise reduction obtained. From the graphs, serrations with height of $2h = 30$ or $2h = 40$ ($\lambda = 15$, and $\lambda = 20$ mm respectively) show maximum noise reduction in the order of 5 dB. Among them, the changes in height and wavelength only modify the frequency where the maximum noise reduction is reached. The results from this figure suggest again that, for maximum noise reduction performance, the ratio $2h/\delta^*$ must be higher than 12. The two highest serration designs ($2h = 30$, and $2h = 40$ mm) have demonstrated the same level of noise reduction, as predicted by the analytical models. However, the smaller serrations ($2h = 20$, and $2h = 10$ mm) present a lower level of noise reduction.

These results are better illustrated in Fig. 13, where a contour of the variation of the noise reduction with the serration scale is shown for $\alpha = 0°$, and $\alpha = 10°$. Fig. 13(a) depicts the predicted cut–on, cut–off and max frequency, based on Eqs. 4, 5, and 7 respectively. As observed, the Strouhal number of maximum trailing–edge noise ($f\delta^*/U_\infty \approx 0.09$) describes well the region where maximum noise reduction is observed. The cut–on frequency, based on the serration wavelength, can also describe the region where noise reduction is higher than 2 dB (3 dB below maximum
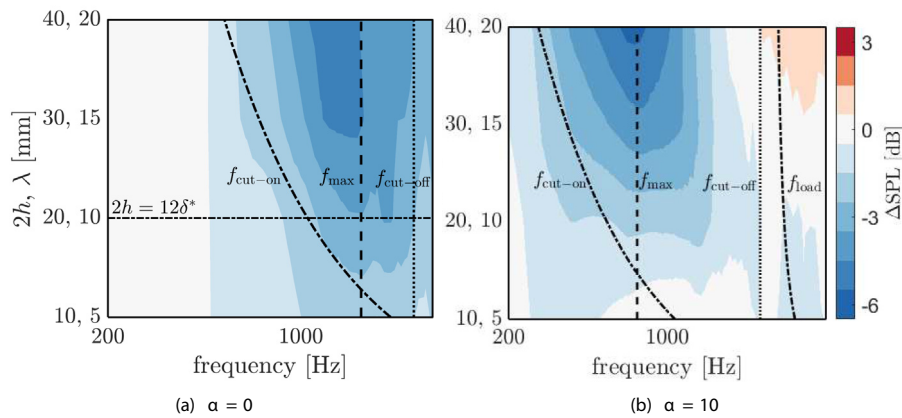
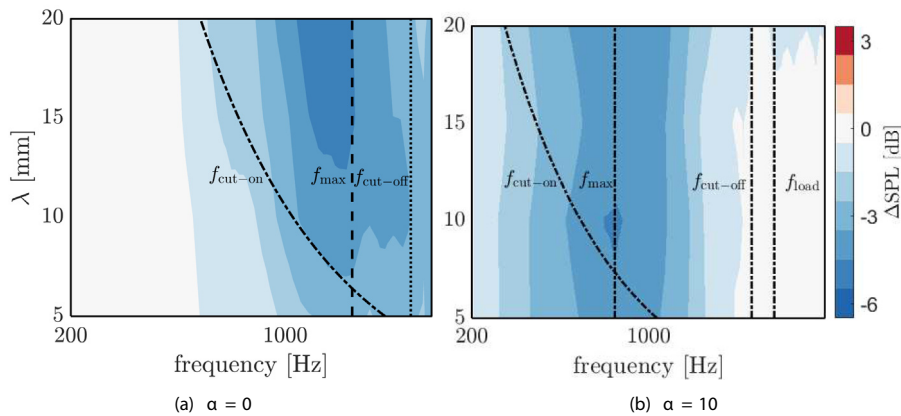**Fig. 13.** Contour plot of the variation of noise reduction for $\alpha = 0°$ (a), and $\alpha = 10°$ (b) at $U_\infty = 30$ m/s with the variation of serration wavelength and height while keeping the aspect ratio constant ($2h/\lambda = 2$). Black lines show the theoretical predictions for the cut–on, max, cut–off, and loading noise frequencies.

Fig. 14. Measured noise reduction (ΔSPL) obtained at $U_\infty = 30$ m/s by varying the serration geometry parameterized with the solidity factor *SF*. (a) $\alpha = 0°$, and (b) $\alpha = 10°$.

noise reduction) for the different wavelengths tested. The cut–off frequency describes the region where noise reduction is decaying below 3 dB. Again, it can be inferred that serrations with small wavelength, such as $\lambda = 5$, and $\lambda = 10$ mm, have a very small frequency range for noise reduction, y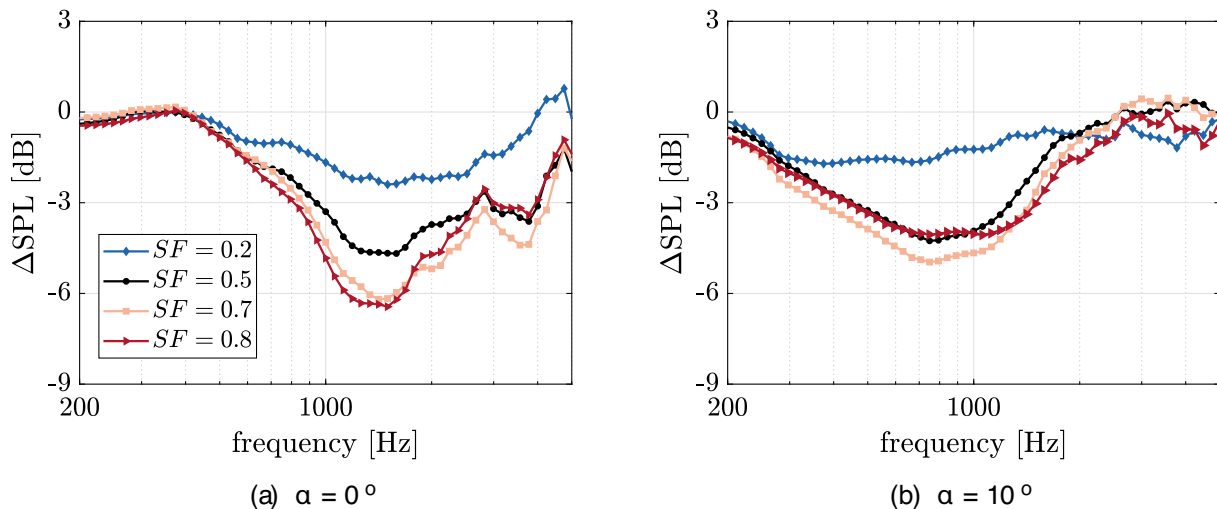ielding poorer performance than expected. As discussed in the previous section, in order to satisfy $f_{\mathrm{cut-on}} < f_{\mathrm{max}}$, the serration wavelength should follow $\frac{\lambda}{\delta^*} > 5$.

The serration height yields a higher sensitivity to the angle of attack, as observed in Figs. 12(b), and 13(b) where noise increasing due to aerodynamic loading is observed for the highest serrations tested. Still, the thicker boundary layer shows the benefits of a larger serration design, achieving higher noise reductions at low frequencies.

4.3. Serration geometry

In this section, the effect of the serration geometry is assessed. Convex and concave–shaped serrations are compared against a baseline sawtooth design. In Fig. 14, the noise reduction spectrum is shown for the different geometries tested. Fig. 14(a) shows the noise reduction at $\alpha = 0°$. The results demonstrate the beneficial effect of the higher serration root angle, as discussed in Ref. [11]. From the experiments, the concave–shaped serrations have shown a reduction of the noise of about 6 dB, compared to 5 dB from the baseline sawtooth. Ref. [11] attributes the better performance of the concave–shaped serrations to the reduced scattering at the root at low frequencies. Ref. [17] also demonstrates that the low–frequency wall–pressure fluctuations are more intense along the serration root. By creating a higher angle at the root, the concave serrations promote a lower scattering at the region where the wall–pressure fluctuations are more intense, yielding a higher noise reduction. On the other hand, the convex design, which features a lower angle at the root in comparison to the other designs, presents a much poorer noise reduction performance. The concave serrations create a more intense scattering at the tip, where high–frequency fluctuations are more intense. As a result, the noise increases faster at high frequencies for $SF = 0.8$ than for $SF = 0.2$ for frequencies above 3000 Hz. Ref. [11] has also observed that the benefits of concave-shaped serrations are limited to the low–frequency region.

Nevertheless, the advantages of the concave serrations at low angles of attack are balanced at high angles of attack. The larger surface area promotes higher aerodynamic loading when concave serrations are placed at 10° angle of attack. This yields a more intense

vortical formation around the edges of the serrations, resulting in a more significant loss of performance at high angles of attack. As a result, the noise reduction obtained at $\alpha = 10°$ (Fig. 14b) shows similar levels for both the sawtooth and concave–shaped serrations. At this condition, the maximum noise reduction is obtained by the serration with $SF = 0.7$, contrary to the $\alpha = 0°$ condition, where the $SF = 0.8$ presented the highest noise reduction. Besides, at high frequencies, the convex–shaped serration shows the best noise reduction in comparison to the other designs. These results suggest that the optimal serration geometry is different depending on the loading condition and while concave shapes are advantageous for low loading conditions, sawtooth–like and even convex–like shapes are preferable for conditions of high angles of attack.

4.4. Combed sawtooth design

This section is dedicated to the observed noise reduction obtained when combs are added to the sawtooth serration design. At first, the focus is given to the number of comb teeth and the thickness of these teeth. Fig. 15 shows the noise reduction spectrum obtained with the different number of teeth (N_{teeth}). From the conditions at a low angle of attack ($\alpha = 0°$), an interesting feature can be observed. None of the combed options (red shades) seems to reduce more noise than the baseline sawtooth (black curve). The results indicate that the introduction of the combs is not beneficial to the serration design. This happens as the tip of the combs are equivalent to a straight trailing edge, and their addition is detrimental to the serration performance, as shown in the analytical work of Ref. [22] for slit–sawtooth serrations. The comb thickness and the number of teeth determine the frequency at which the combed–sawtooth noise reduction departs from the sawtooth one. Thicker combs present a noise reduction curve that deviates from the sawtooth one at lower frequencies. This departure is clear in the figure as $N_{\mathrm{teeth}} = 1$ is less effective than the sawtooth design for $f > 500$ Hz, $N_{\mathrm{teeth}} = 3$ for $f > 1000$ Hz, $N_{\mathrm{teeth}} = 5$ for $f > 1500$ Hz, and $N_{\mathrm{teeth}} = 7$ for $f > 2000$ Hz. This corresponds to a Strouhal number based on the comb thickness ($St = ft_{\mathrm{teeth}}/U_\infty$) around 0.05.

In summary, without the presence of aerodynamic loading, the results indicate that the thinner the combs on the serration are, the more similar the noise reduction is to the regular sawtooth design. The sawtooth serration represents the limit where $t_{\mathrm{comb}} = 0$ mm
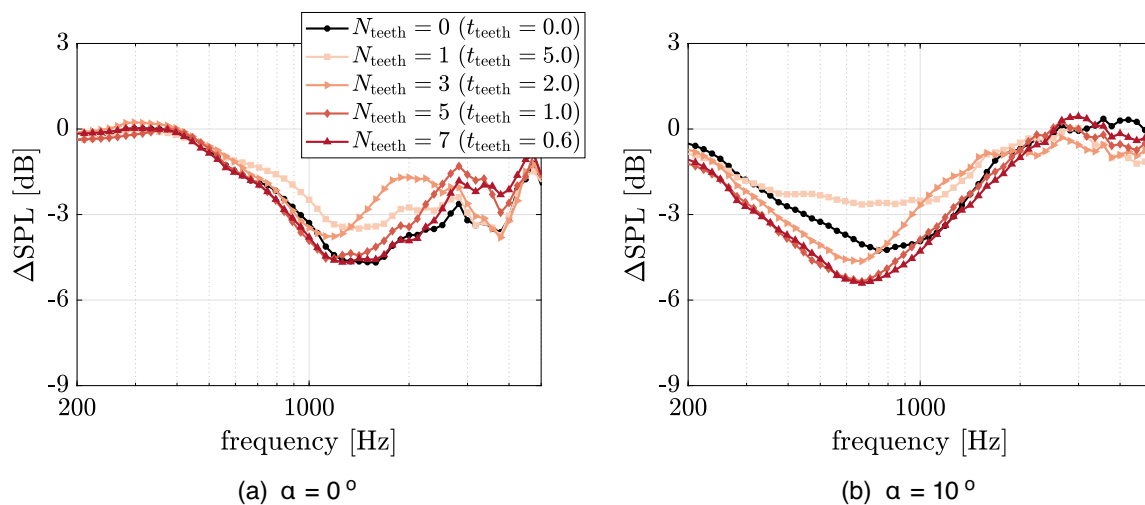

Fig. 15. Measured noise reduction (ΔSPL) obtained at $U_\infty = 30$ m/s by varying the number of combs (N_{teeth}) in the combed sawtooth design. (a) $\alpha = 0°$, and (b) $\alpha = 10°$.

and it reduces the noise the most in comparison to other combed–sawtooth designs.

These results differ from literature [12] and applied combed–sawtooth serrations on an industrial environment [2], which indicate a significantly better performance of the combed sawtooth concept in comparison with the sawtooth design. A reason for the discrepancies is seen when observing the noise reduction at $\alpha = 10°$. At this condition, the combed–sawtooth designs with $N_{\text{teeth}} \geqslant 3$ present a higher noise reduction than the sawtooth one. Based on previous studies [12,16,17], it is expected that the presence of the combs avoid the formation of the counter–rotating pair of vortices, in turn avoiding the secondary wall–pressure fluctuations observed when sawtooth serrations are placed under aerodynamic loading. Besides, by extending the region of scattering further downstream, the combs also decrease low–frequency noise, with a mechanism similar to the concave serrations, where the scattering happens in the region of lowest wall–pressure fluctuations.

It is important to highlight that the benefits of the combed–sawtooth design are extended for serrations placed at large angles with respect to the airfoil trailing–edge angle. For example, Ref. [12] demonstrates a better noise reduction from the combed–sawtooth compared to the standard sawtooth serrations mounted on a NACA 0018 airfoil at zero angle of attack. This airfoil shape features a 12° angle between the trailing edge and the airfoil chord line. The work shows that the combs greatly reduce the spanwise deviation of the flow along the serration. In that sense, the combs are a solution to avoid any secondary flow formation along the serration, in turn, creating a design that is more robust to serration installation and aerodynamic loading from changing angles of attack. From the graphs at $\alpha = 10°$, it is possible to observe that the designs with $N_{\text{teeth}} = 5$, and $N_{\text{teeth}} = 7$ reduce up to 1 dB more noise than the regular sawtooth design.

A second analysis investigates how the solidity factor of the combed serration affects the performance at low and high angles of attack. The serrations tested have 5 teeth per wavelength ($N_{\text{teeth}} = 5$) and are differentiated by the thickness of these teeth, respectively $t_{\text{teeth}} = 0.6, 1.0$, and 2.0 mm. To achieve these teeth thicknesses, the gap in-between teeth is $2.0, 1.0$, and 0.6 mm respectively. The baseline sawtooth serration is also shown as a reference result, which is equivalent to $t_{\text{teeth}} = 0$ mm. Fig. 16 shows the noise reduction spectrum at two angles of attack. By increasing the comb thickness, the scattering is moved to the tip of the serra-

tions, resulting in a higher noise reduction at low frequencies, as observed in Fig. 16(a) for $\alpha = 0°$. However, following the previous discussions, this benefit is missed at high frequencies, where the thicker combs present a cut-off at lower frequencies.

Still, the main differences are observed for $\alpha = 10°$, where the aerodynamic loading is responsible for decreasing the noise reduction at high frequencies of the serrations. Under these conditions, the serration with $t_{\text{teeth}} = 1.0$ mm ($SF = 0.75$) presents the best compromise between noise reduction at low frequencies and no increase in noise at high frequencies.

Results suggest that the combs are effective in avoiding the secondary flow features induced by the pressure difference over the serration surface, creating a design that can reduce noise at different conditions of angles of attack, airfoil cambers, and wedge angle between the airfoil and the serration surfaces. However, introducing the combs cause the noise reduction curve to have a lower cut–off frequency, in turn reducing the overall noise reduction from the serration to the sawtooth design. It is expected that the comb size must follow $t_{\text{teeth}} < 0.05 U_\infty / f_{\text{cut–off}}$ to avoid this cut–off to affect the noise reduction. The comb pitch and solidity are another important way of controlling the noise reduction obtained. From the results, the thicker combs ($t_{\text{teeth}} = 1.0$ mm, and $t_{\text{teeth}} = 2.0$ mm) are the most effective ones at high angles. Nevertheless, the thicker the comb the worse the noise reduction performance is at high frequencies.

5. Summary of parameter dependence

This work provides guidelines for the design of trailing–edge serrations. The following paragraphs summarize the results obtained and the impacts expected for each parameter varied in this study:

$2h/\delta^*$: the serration height governs the maximum noise reduction obtained. This is hypothesized in Ref. [5]. However, following Ref. [20], a limit is observed for serrations of a certain height. In this work, a maximum noise reduction is reached for serrations of $2h/\delta^* \gtrsim 12$. Results indicate that this value is an optimum for noise reduction, above which no significant improvement is observed. Also, the height of the serration influences its performance at high angles of attack. Results and theory indicate that the serration height influences the frequency and levels where the aerodynamic loading modifies the noise from the serrations. For high
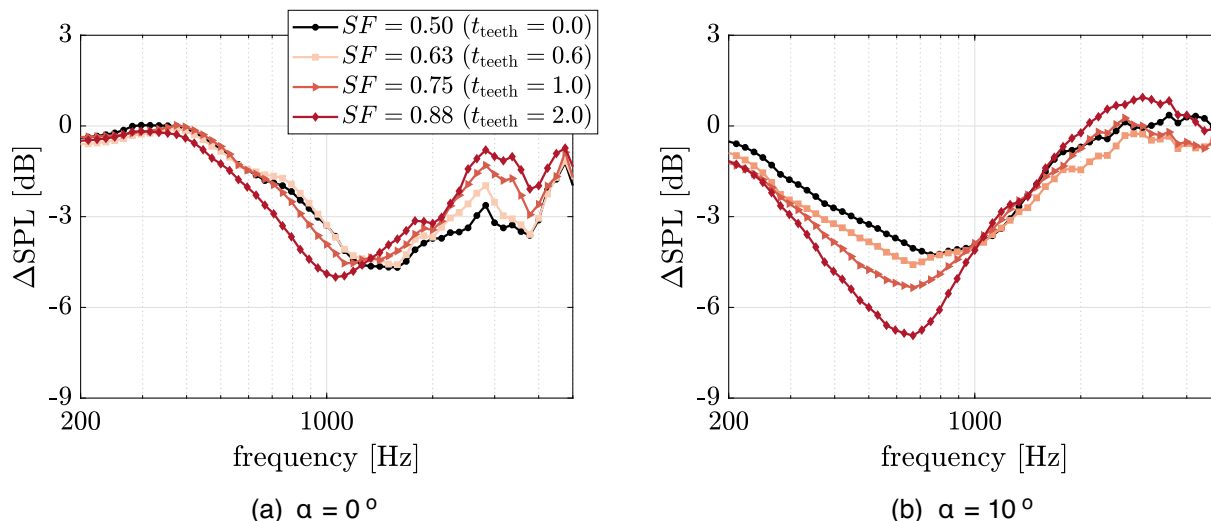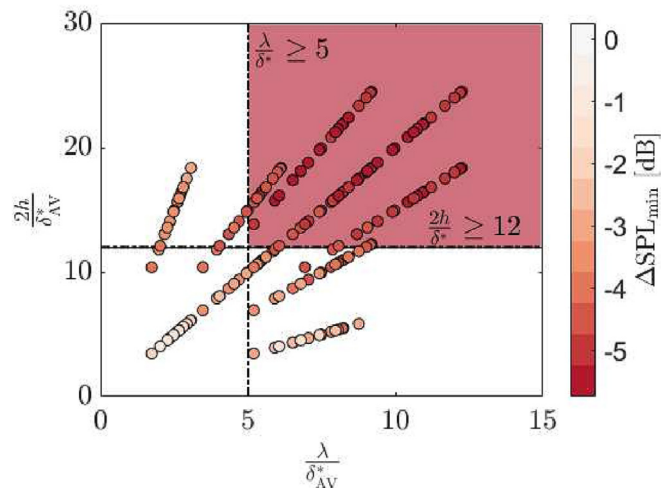

Fig. 16. Measured noise reduction (ΔSPL) obtained at $U_\infty = 30$ m/s by varying the solidity factor (SF) of the combs in the combed sawtooth design. (a) $\alpha = 0°$, and (b) $\alpha = 10°$.

Fig. 17. Summary scatter plot of maximum noise noise reduction ΔSPL_{min} for all sawtooth geometries tested under all angle of attack and flow speed conditions available. The graph also depicts the two criteria for serration design mentioned in this work, i.e. $2h/\delta^* \gtrsim 12$, and $2h/\delta^* \gtrsim 5$.

$2h/\delta^*$ serrations, the increase of the noise levels due to aerodynamic loading is stronger, and results from this work have demonstrated up to 3 dB noise increase at $10°$ angle of attack.

λ/δ^*: the serration wavelength affects mostly the frequency where noise reduction is observed. This is first noted in this work and, according to the theoretical models, the cut–on frequency is inversely proportional to the serration wavelength. Nevertheless, the frequency of cut–off, and of maximum noise reduction are independent of the wavelength. As a consequence, small wavelength serrations reduce noise in a narrower range of frequencies and, at some conditions, cannot reach the maximum noise reduction expected. This is observed in the results where excessively narrow serrations do not reduce noise as wider ones. Considering that the cut–on frequency is desirably below the frequency of maximum generation of broadband noise, the serration wavelength should follow $\frac{\lambda}{\delta^*} \gtrsim 5$. The wavelength does not modify the aerodynamic loading, and results at angle of attack seem to collapse into a similar noise reduction spectrum, indicating that the height of the serration is a more important parameter as long as performance under aerodynamic loading is concerned.

$2h/\lambda$: the serration aspect ratio combines the effect of modifying the wavelength and the height of the serration. Unlike described in Ref. [5], increasing the aspect ratio does not necessarily translate into lower noise as alterations of the turbulent flow affect the scattered noise. First, the high–frequency cut-off imposed by the acceleration of the small scales of turbulence limits the noise reduction at certain frequencies. By combining the criteria proposed in the previous two paragraphs, results suggest that an aspect ratio around 2.4 is a valid design as long as both conditions are met concerning the boundary–layer displacement thickness. Besides, the aspect ratio is associated with the sensitivity to the aerodynamic loading. A high aspect ratio serration design is more prone to increasing noise at high frequencies in conditions where the angle between the serrations and the flow direction is high. In this work, meaningful degradation of the high–frequency performance is observed for angles above $10°$ when considering the sum of the angle of attack (α), the airfoil camber (θ_{TE}), the trailing–edge angle (δ_{TE}), and the serration flap angle with respect to the chord line (δ_{Serr}), i.e. $\alpha + \theta_{TE} + \delta_{TE} + \delta_{Serr} > 10$.

Fig. 17 summarizes all the modifications of the sawtooth geometry and the impact on the maximum noise reduction (ΔSPL_{min}) achieved. The graph combines the results from every sawtooth ser-

ration design, angle of attack, and flow speed assessed. The region of $2h/\delta^* \geqslant 12$, and $\frac{\lambda}{\delta^*} \geqslant 5$ is also shown, demonstrating that it contains the designs that achieve maximum noise reduction for this experiment.

Concave-shaped serrations: the concave–shaped serrations have demonstrated higher noise reduction in comparison to the sawtooth design, as also observed in Ref. [11]. The higher serration angles at the root are responsible for a lower scattering at this region. Refs. [17,11,12] have shown that the low–frequency wall–pressure fluctuations are more intense at the serration root. It is expected that the less intense scattering at the region of the strongest wall–pressure fluctuations is the underlying phenomenon responsible for the better performance of concave–shaped serrations. On the other hand, the concave–shaped serrations feature a lower angle at the tip. The same Refs. [17,11,12] have also demonstrated that high–frequency wall–pressure fluctuations increase at the tip of the serration. This restricts the advantages of concave–shaped serrations at this frequency range. Besides, the higher associated solidity factor in comparison to the sawtooth serrations is related to a poorer behaviour of the high–frequency noise reduction at angles of attack.

Serration combs: combs are an important feature to reduce secondary flow formations that affect the serration noise. This reduction yield a design that is more robust concerning airfoil camber, angle of attack, and serration wedge angle. It is shown here that, at angles of attack of $10°$, the combed serrations reduce as much as 2 dB more noise than the sawtooth design. Nevertheless, the thickness of the comb modifies the high–frequency noise at low angles of attack. It is shown that this thickness is associated with an early cut–off of the noise reduction at non–dimensional frequencies beyond $ft_{combs}/U_\infty = 0.05$. At higher frequencies, the presence of the combs causes an increase in the noise. This is related to the more intense scattering along the straight edges of the combs. Regarding the thickness of the combs with respect to the gap between them, the results point to an optimal region where the thickness of the combs equals the width of these gaps. Thicker combs yield an increase of noise at high frequencies while smaller ones yield similar behaviour to the sawtooth serrations.

The analysis presented in this work has focused on the acoustic properties of trailing-edge serrations. The implementation of these devices, however, also impacts the aerodynamic properties of the serrated airfoil, e.g. modifications of the lift and drag of the airfoil. Concerning this increase, serration add-ons increase the area of the airfoil section by $\Delta A_{serration} = SF.b.2h$, where b is the model span. Therefore, by increasing the solidity factor (SF) or the height of the serrations ($2h$), it is expected that the serration contribution to drag and lift should also increase. This criterion can possibly limit the application of excessively large serrations, concave-shaped serrations, or thick combs.

6. Conclusions

This work describes a parametric study of trailing–edge serrations for turbulent boundary layer trailing–edge noise. Several geometries are experimentally tested and results are used to assess the design choices of serration scaling and geometry on the noise reduction obtained. The study is carried out with a one–factor–a t–a–time procedure proposed to individually assess the influence of each design parameter on the noise reduction achieved. A series of design modifications are given to a reference sawtooth serration geometry to describe the sensitivity of this design with respect to modifications of the serration height, wavelength, aspect ratio, and of the serration geometry, represented by concave and combed-sawtooth designs. A summary of the main obtained trends is presented, culminating in a guideline on serration design for

broadband noise reduction. Two independent physical phenomena are used to carry the discussion about the effects of serration design on noise, namely the acoustic scattering, and the influence on the turbulent flow surrounding the serration. The latter is separated between effects that are observed when serrations are placed at an angle with respect to the flow direction and effects that are present at every condition. The conclusions obtained in this work can be used as a practical guideline for the preliminary design and sizing of serrations for different applications.

CRediT authorship contribution statement

Lourenço Tércio Lima Pereira: Conceptualization, Methodology, Data curation, Writing - original draft, Writing - review & editing. **Francesco Avallone:** Conceptualization, Methodology, Writing - review & editing. **Daniele Ragni:** Conceptualization, Methodology, Writing - review & editing. **Fulvio Scarano:** Conceptualization, Methodology, Writing - review & editing.

Data availability

Data will be made available on request.

Declaration of Competing Interest

The authors declare that they have no known competing financial interests or personal relationships that could have appeared to influence the work reported in this paper.

References

[1] Oerlemans S, Fisher M, Maeder T, Kögler K. Reduction of Wind Turbine Noise Using Optimized Airfoils and Trailing-Edge Serrations. AIAA Jurnal 2009;47 (6):1470–81. https://doi.org/10.2514/1.38888. URL: http://arc.aiaa.org/doi/10.2514/1.38888.

[2] Asheim MJ, Ferret O Gasch, Oerlemans S, Rotor blade with a serrated trailing edge (2017).

[3] Ye X, Zheng N, Zhang R, Li C. Effect of serrated trailing-edge blades on aerodynamic noise of an axial fan. J Mech Sci Technol 2022;36(6):2937–48. https://doi.org/10.1007/s12206-022-0526-7.

[4] Howe M. Aerodynamic noise of a serrated trailing edge. J Fluids Struct 1991;5 (1):33–45. https://doi.org/10.1016/0889-9746(91)80010-B. URL: https://linkinghub.elsevier.com/retrieve/pii/088997469180010B.

[5] Howe MS. Noise produced by a sawtooth trailing edge. J Acoust Soc Am 1991;90(1):482–7. https://doi.org/10.1121/1.401273.

[6] Lyu B, Azarpeyvand M, Sinayoko S. Prediction of noise from serrated trailing edges. J Fluid Mech 2016;793:556–88. https://doi.org/10.1017/jfm.2016.132. arXiv:1508.02276.

[7] Ayton LJ. Analytic solution for aerodynamic noise generated by plates with spanwise-varying trailing edges. J Fluid Mech 2018;849(August):448–66. https://doi.org/10.1017/jfm.2018.431.

[8] Lyu B, Ayton LJ. Rapid noise prediction models for serrated leading and trailing edges. J Sound Vib 2020;469:. https://doi.org/10.1016/j.jsv.2019.115136. arXiv:1906.02645115136.

[9] Grasso G, Roger M, Moreau S, Effect of sweep angle and of wall-pressure statistics on the free-field directivity of airfoil trailing-edge noise, 25th AIAA/CEAS Aeroacoustics Conference, 2019 (May) (2019) 1–16. doi:10.2514/6.2019-2612.

[10] Arce León C, Ragni D, Pröbsting S, Scarano F, Madsen J. Flow topology and acoustic emissions of trailing edge serrations at incidence. Exp Fluids 2016;57 (5). https://doi.org/10.1007/s00348-016-2181-1.

[11] Avallone F, van der Velden WC, Ragni D. Benefits of curved serrations on broadband trailing-edge noise reduction. J Sound Vib 2017;400(April):167–77. https://doi.org/10.1016/j.jsv.2017.04.007.

[12] Avallone F, van der Velden WC, Ragni D, Casalino D. Noise reduction mechanisms of sawtooth and combed-sawtooth trailing-edge serrations. J Fluid Mech 2018;848(June):560–91. https://doi.org/10.1017/jfm.2018.377.

[13] Gruber M, Airfoil noise reduction by edge treatments by Mathieu Gruber Thesis for the degree of Doctor of Philosophy (2012).

[14] Chong TP, Vathylakis A. On the aeroacoustic and flow structures developed on a flat plate with a serrated sawtooth trailing edge. J Sound Vib 2015;354:65–90. https://doi.org/10.1016/j.jsv.2015.05.019.

[15] Avallone F, Pröbsting S, Ragni D. Three-dimensional flow field over a trailing-edge serration and implications on broadband noise. Phys Fluids 2016;28(11). https://doi.org/10.1063/1.4966633.

[16] Lima Pereira LT, Avallone F, Ragni D, Wall-pressure fluctuations over a serrated trailing edge at different angles of attack, in: AIAA/CEAS Aeroacoustics Conference, 2021, pp. 1–15. doi:10.2514/6.2021-2179.

[17] Lima Pereira LT, Avallone F, Ragni D, Scarano F. A physics-based description and modelling of the wall-pressure fluctuations on a serrated trailing edge. J Fluid Mech 2022;938:A28. https://doi.org/10.1017/jfm.2022.173. URL: https://www.cambridge.org/core/product/identifier/S0022112022001732/type/journal_article.

[18] Ayton LJ, Szoke M, Paruchuri CC, Devenport WJ, Alexander WN. Trailing-edge serrations: improving theoretical noise reduction models. In: AIAA AVIATION 2021 FORUM, American Institute of Aeronautics and Astronautics, Reston, Virginia. https://doi.org/10.2514/6.2021-2111.

[19] Lima Pereira LT, Ragni D, Avallone F, Scarano F. Aeroacoustics of sawtooth trailing-edge serrations under aerodynamic loading. J Sound Vib 2022;537:. https://doi.org/10.1016/j.jsv.2022.117202. https://linkinghub.elsevier.com/retrieve/pii/S0022460X22003960117202.

[20] Gruber M, Joseph P, Chong T, On the mechanisms of serrated airfoil trailing edge noise reduction, 17th AIAA/CEAS Aeroacoustics Conference (32nd AIAA Aeroacoustics Conference) (June) (2011) 5–8. doi:10.2514/6.2011-2781. URL: http://arc.aiaa.org/doi/10.2514/6.2011-2781.

[21] Kholodov P, Moreau S. Optimization of trailing-edge serrations with and without slits for broadband noise reduction. J Sound Vib 2020;490:. https://doi.org/10.1016/j.jsv.2020.115736115736.

[22] Azarpeyvand M, Gruber M, Joseph P, An analytical investigation of trailing edge noise reduction using novel serrations, 19th AIAA/CEAS Aeroacoustics Conference (2013) 1–17 doi:10.2514/6.2013-2009. URL: http://arc.aiaa.org/doi/10.2514/6.2013-2009.

[23] Moreau DJ, Doolan CJ. Noise-Reduction Mechanism of a Flat-Plate Serrated Trailing Edge. AIAA J 2013;51(10):2513–22. https://doi.org/10.2514/1.j052436.

[24] Luesutthiviboon S, Lima Pereira LT, Ragni D, Avallone F, Snellen M. Aeroacoustic Benchmarking of Trailing-edge Noise from a NACA63₃–018 Airfoil with Trailing-edge Serrations. Accepted for publication on AIAA Journal on the August 2022.

[25] Merino-Martínez R, Rubio Carpio A, Lima Pereira LT, van Herk S, Avallone F, Ragni D, Kotsonis M. Aeroacoustic design and characterization of the 3D-printed, open-jet, anechoic wind tunnel of Delft University of Technology. Appl Acoust 2020;170. https://doi.org/10.1016/j.apacoust.2020.107504.

[26] Bailey SC, Hultmark M, Monty JP, Alfredsson PH, Chong MS, Duncan RD, Fransson JH, Hutchins N, Marusic I, McKeon BJ, Nagib HM, Örlü R, Segalini A, Smits AJ, Vinuesa R. Obtaining accurate mean velocity measurements in high Reynolds number turbulent boundary layers using Pitot tubes. J Fluid Mech 2013;715:642–70. https://doi.org/10.1017/jfm.2012.538.

[27] Sijtsma P, Phased Array Beamforming Applied to Wind Tunnel and Fly-Over Tests, SAE Technical Papers 2010-Octob (October) (2010) 17–19. doi:10.4271/2010-36-0514.

[28] Sarradj E, Fritzsche C, Geyer T, Giesler J. Acoustic and aerodynamic design and characterization of a small-scale aeroacoustic wind tunnel. Appl Acoust 2009;70(8):1073–80. https://doi.org/10.1016/j.apacoust.2009.02.009.

[29] Lima Pereira LT, Merino-martínez R, Ragni D, Gómez-ariza D. Combining asynchronous microphone array measurements for enhanced acoustic imaging and volumetric source mapping. Appl Acoust 2021;182. https://doi.org/10.1016/j.apacoust.2021.108247.

[30] Taylor GI, The Spectrum of Turbulence, Proceedings of the Royal Society of London. Series A - Mathematical and Physical Sciences 164 (919) (1938) 476–490. doi:10.1098/rspa.1938.0032. URL: http://www.royalsocietypublishing.org/doi/10.1098/rspa.1938.0032.

[31] Chong TP, Joseph PF, Davies PO. Design and performance of an open jet wind tunnel for aero-acoustic measurement. Appl Acoust 2009;70(4):605–14. https://doi.org/10.1016/j.apacoust.2008.06.011.

[32] Sanjosé M, Moreau S, Lyu B, Ayton LJ, Analytical, numerical and experimental investigation of trailing-edge noise reduction on a Controlled Diffusion airfoil with serrations, 25th AIAA/CEAS Aeroacoustics Conference (May) (2019). doi:10.2514/6.2019-2450. URL: https://arc.aiaa.org/doi/10.2514/6.2019-2450.

[33] Hwang YF, Bonness WK, Hambric SA. Comparison of semi-empirical models for turbulent boundary layer wall pressure spectra. J Sound Vib 2009;319(1–2):199–217. https://doi.org/10.1016/j.jsv.2008.06.002.

[34] Arce León C, Ragni D, Pröbsting S, Scarano F, Madsen J. Flow topology and acoustic emissions of trailing edge serrations at incidence. Exp Fluids 2016;57 (5). https://doi.org/10.1007/s00348-016-2181-1.

[35] Romani G, Casalino D, van der Velden W. Numerical analysis of airfoil trailing-edge noise for straight and serrated edges at incidence. AIAA J 2021;59 (7):2558–77. https://doi.org/10.2514/1.J059457.

[36] Arce León C, Merino-Martínez R, Ragni D, Avallone F, Snellen M. Boundary layer characterization and acoustic measurements of flow-aligned trailing edge serrations. Exp Fluids 2016;57(12):1–22. https://doi.org/10.1007/s00348-016-2272-z.

[37] Brooks MA, Pope TF, Marcolini DS, Airfoil self-noise and prediction (August 1989) (1989).